ELSEVIER

PII: S0032-3861(96)01080-4

Polymer Vol. 38 No. 18, pp. 4595–4607, 1997

0032-3861/97/$17.00+0.00

Macromolecular dynamics in extensional flows: 2. The evolution of molecular strain

S. P. Carrington, J. P. Tatham and J. A. Odell*
H. H. Wills Physics Laboratory, University of Bristol, Bristol BS8 1TL, UK

and A. E. Sáez
Department of Chemical Engineering, North Carolina State University, Raleigh, NC 27695-7905, USA
(Received 24 June 1996)

The opposed jets apparatus has been used to investigate the dynamics of the coil–stretch transition of polymer solutions in an idealized stagnation point extensional flow field. Flow simulations generated fluid strain profiles for different geometries. Assuming a molecular uncoiling model, true birefringence profiles have been converted to molecular strains for closely monodisperse, high molecular weight aPS under θ-conditions. This has enabled macromolecular deformation to be followed as a function of position and residence time. Non-linear hydrodynamic friction FENE dumb-bell simulations give qualitative agreement. Initially, molecular uncoiling is non-affine, consistent with changing hydrodynamic screening on extension. Deformation in a good solvent is more affine. Results are compared with PEO/water to investigate the effect of molecular parameters. The effective extensional viscosity has been ascertained by correction for the area of high molecular extension. The increase in extensional viscosity due to molecular stretching is substantial, of the order of the number of equivalent flexible units in the chain. © 1997 Elsevier Science Ltd.

(Keywords: molecular stretching; polymer solutions; extensional flow)

INTRODUCTION

Polymer solutions typically exhibit non-Newtonian flow behaviour. In extensional flows, this is usually manifested as 'extension thickening'—a dramatic viscosity increase with flow rate. Many real flows of commercial importance contain significant extensional components. Considerable theoretical and experimental research has been directed at studying the response of polymer molecules to stretching flows, and in turn, assessing the effect which extending molecules have on the applied flow field. The transition of a macromolecular coil to an extended conformation may be studied in an idealized extensional flow field, such as that generated by the opposed jets apparatus.

In part one of this work, we have presented results from an opposed jets apparatus which incorporated design improvements to realize better flow control and much improved spatial resolution of flow induced retardation around the stagnation point[1]. The use of an iterative numerical transform permitted the recovery of absolute birefringence as a function of radial position. The birefringence profiles indicated the presence of pronounced screening effects at all but the lowest concentrations. Such effects arise from the local increase in extensional viscosity producing significant flow modification with a reduced strain rate around the stagnation point. The screening was particularly severe for high molecular weights and good solvents.

At concentrations low enough to be considered truly dilute ($\approx c^*/100$), a well-behaved birefringent strand, highly localized around the stagnation point, was observed. The onset of stretching occurred at a critical strain rate and showed a sigmoidal profile with increasing strain rate. The width of the transition was consistent with the known polydispersity of the polymers used. The final plateau levels of birefringence were of the same order as the theoretical values expected for fully oriented polymers, including form birefringence but subject to the uncertainties of solvent effects.

After allowance for the area of strongly birefringent molecules, the effective extensional viscosity showed an enormous increase ($\approx$1000 fold) during the stretching transition. This was of the order of N, the number of equivalent flexible links in the chain.

The above observations point to a critical coil–stretch transition with a high degree of stretching of the molecules around the stagnation point. In this paper, we convert birefringence profiles to molecular strain profiles by assuming a model for the uncoiling process of polymer molecules in a stagnation point extensional flow field. This model is applied to the well behaved birefringence profiles obtained in the absence of flow modification. The generation of molecular strain profiles enables the increase in effective extensional viscosity to be reassessed allowing for the area of highly stretched molecules.

Modelling of the flow field in potential and viscous regimes is used to follow the evolution of fluid strain. The subsequent comparison of molecular and fluid strains

* To whom correspondence should be addressed

allows the macromolecular dynamics to be examined in a quasi-steady state flow field.

EXPERIMENTAL

Apparatus

The opposed jets apparatus allows simultaneous optical birefringence and flow resistance measurements, enabling the correlation of molecular orientation with its effect upon the flow field[2]. The apparatus used in this work, incorporating a linear CCD (Charge Coupled Device) array to record intensity profiles across the birefringent lines, has been described previously[1].

Polymer samples

The aPS samples used in these experiments were closely monodisperse (polydispersity index = 1.05–1.2), supplied and characterized by Polymer Laboratories (Church Stretton, UK). Decalin is a θ solvent for aPS close to room temperature, and has a viscosity of 0.0024 Pa s^{-1} at 20°C. TCP is a good solvent for aPS at room temperature[3], and the commercial mix of isomers was found to have a viscosity of 0.051 Pa s^{-1} at 23°C. The increased viscosity of TCP, compared to decalin, would be expected to reduce inertial effects in the flow field. The PEO sample used had a peak molecular weight, $M_p = 1.39 \times 10^6$, and was closely monodisperse, with $M_w/M_n = 1.15$. The sample was supplied and characterized by Polymer Laboratories. For the relevant molecular weight range, the Mark–Houwink exponent, $a = 0.76$[4]. The solution preparation techniques have been described previously[1].

Flow field analysis

To a first approximation, the flow field created by sucking fluid into two opposed jets has been considered to be uniaxial extension with a nominal strain rate, $\dot{\epsilon}_{nom}$, at volume rate, Q, defined as[2,5,6]:

$$\dot{\epsilon}_{nom} = \frac{Q}{Ad} \tag{1}$$

where A is the area of each jet and d is the jet separation. A pure uniaxial extensional flow would have a constant strain rate throughout. A stagnation point is generated on the mid-point of the axis joining the two jet apertures, about which there is cylindrical symmetry.

Mackley found that the theoretical streamlines for an equivalent uniaxial extensional flow did not match closely the observed streamlines[7]. The real flow contains a 'nip' point (usually situated just outside the jets), at which the flow field changes sign from convergent to divergent. This limits the fluid strain that can be accumulated on passage through the jets. Indeed, a pure uniaxial extension would accumulate unlimited strain on the incoming symmetry plane, in qualitative disagreement with the observations of narrow birefringent strands along the exit symmetry axis. Mackley attempted to model the flow field in terms of two 'point sinks' placed near to each other.

Schunk *et al.* solved the Navier–Stokes and continuity equations by finite element analysis, and produced numerical simulations of the opposed jet flow field[8]. They reported reasonable agreement with experimental measurements for Newtonian fluids at low Reynolds numbers[9].

Two computer simulations of the opposed jets flow field applicable to the flow regime used in this laboratory have been developed.

High Reynolds number simulation. At high Reynolds number the viscous terms can be neglected in the Navier–Stokes equations. For potential flow with cylindrical symmetry, the stream function satisfies the differential equation[10]

$$r\frac{\partial}{\partial r}\left(\frac{1}{r}\frac{\partial \Psi}{\partial r}\right) + \frac{\partial^2 \Psi}{\partial z^2} = 0 \tag{2}$$

where the stream function is defined by

$$v_z = -\frac{1}{r}\frac{\partial \Psi}{\partial r}, \quad v_r = \frac{1}{r}\frac{\partial \Psi}{\partial z} \tag{3}$$

where v_z and v_r are the components of the velocity field in the axial and radial directions respectively. The boundary conditions applicable to this problem are shown in *Figure 1*. All lines of symmetry and solid surfaces are boundaries with constant stream function. However, the condition at $z = L$ inside the capillary is a developed flow condition, with $v_r = 0$ being implicated here. A value of $L = 2\delta$ is sufficient to ensure that flow perturbations within the capillary (arising from the external flow field) have been damped out. A finite element algorithm has been used to solve the differential equation (2).

Low Reynolds number simulation. The viscous flow regime has also been simulated, using the finite element program FIDAP. The simulation of this flow regime

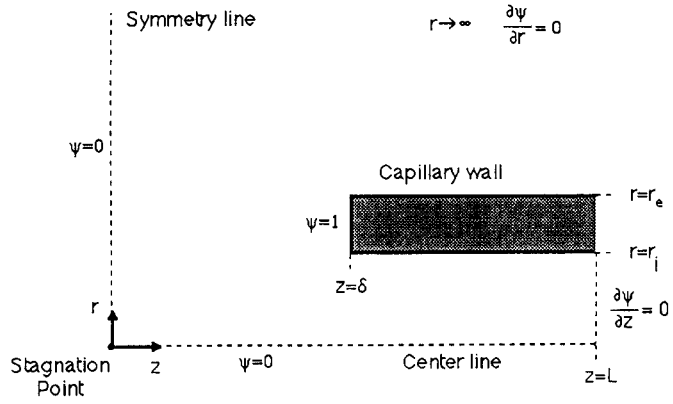

Figure 1 Boundary conditions for the opposed jets flow field simulation

corresponds to the solution of the Stokes equations, and inertial effects are negligible in this case.

A nominal strain rate of $1000\,s^{-1}$ was chosen for this simulation, which gives a flow analysis for the low Reynolds number case. These flow results can be scaled to other velocities in the viscous flow regime, since the normalized velocity is independent of fluid properties.

Birefringence analysis and derivation of molecular strain

As previously shown, data representing birefringence, Δn, as a function of radial distance from the symmetry axis, r, can be obtained from CCD measurements[1,11,12]. The accumulated fluid strain, ϵ, as a function of $(r - r_o)$, where r_o is the radius value at which $\dot{\epsilon}_c$ was first attained, can be obtained from the flow field simulations. The comparison of molecular strain with fluid strain requires a relationship between Δn and molecular strain to be derived.

Birefringence is a measure of the segmental orientation, rather than the molecular strain. However, the stretching of a molecule in an extensional flow field is likely to produce birefringence that is a monotonic function of molecular strain. The two parameters can be related if information concerning the most probable orientation of segments during molecular uncoiling is available.

We will use a model described by Treloar, based on rubber elasticity theory, which derives the optical properties of a strained network[13]. Consider a single flexible chain consisting of n segments, each of length, ℓ, between two cross-links. The chain is held with its ends separated by a vector distance, r. Kuhn and Grün derived the statistical distribution of link angles, measured with respect to the direction of r[14]. The longitudinal and transverse polarizabilities of the chain are denoted by γ_1 and γ_2 (respectively), and a relationship between optical anisotropy of the chain and the end-to-end distance, r, is shown to be

$$(\gamma_1 - \gamma_2) = n(\alpha_1 - \alpha_2)\left\{1 - \frac{3r/n\ell}{\mathcal{L}^{-1}(r/n\ell)}\right\} \qquad (4)$$

where α_1 and α_2 are the longitudinal and transverse polarizabilities of a single segment. $\mathcal{L}^{-1}$ is the inverse Langevin function.

The application of the Lorentz–Lorenz formula and a numerical approximation to $\mathcal{L}^{-1}$ results in

$$\frac{\Delta n}{\Delta n_o} = \frac{3}{5}\left(\frac{r}{n\ell}\right)^2 + \frac{1}{5}\left(\frac{r}{n\ell}\right)^4 + \frac{1}{5}\left(\frac{r}{n\ell}\right)^6 \qquad (5)$$

Equation (5) is shown in graphical form by *Figure 2*. This relation can be solved for the fractional extension, $r/n\ell = \beta$, using the Newton–Raphson method, providing Δn_o is known. Molecular strain, t, is then calculated by

$$t = \frac{r}{\langle r_o^2\rangle^{1/2}} = \frac{r}{n\ell}\frac{n\ell}{\langle r_o^2\rangle^{1/2}} \qquad (6a)$$

$$\text{i.e.} \quad t = \beta t_{max} \qquad (6b)$$

where t_{max} is the strain to full extension [the ratio between the contour length, $n\ell$, and the r.m.s. end-to-end distance of a Gaussian chain, $\langle r_o^2\rangle^{1/2}$].

This model implies that the mean molecular segmental orientation (denoted by the end-to-end separation, r), during each stage of uncoiling in the flow field, is consistent with that of a molecule in stationary solution whose ends are fixed at a distance, r, apart. This is unlikely to be strictly correct because extra factors are produced by the moving solvent, which counter the maximum entropy description. Therefore, this model is likely to produce an overestimate of t.

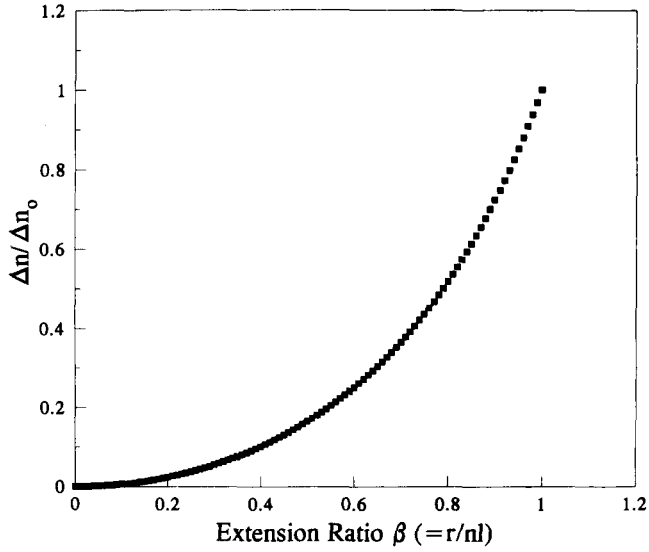

Figure 2 Normalized birefringence *versus* fractional molecular extension (as modelled by Treloar[13])

Several other authors have formulated models of the uncoiling process. Peterlin has calculated birefringence *versus* extension results similar to those of Treloar[15]. The yo-yo model of Ryskin is likely to produce a birefringence vs. extension curve very different to that of the Treloar model[16].

Rallison and Hinch[17], Wiest *et al.*[18], Larson[19] and Hinch[20] have predicted kinks and hairpin folds during the uncoiling process, based on computer simulations. Ultimately, the completely extended chain conformation is reached, but birefringence values close to Δn_o could obviously occur at relatively low molecular strains. However, the kinks dynamics simulations are for extremely high flow strengths which are not appropriate for the flow regime that exists in our opposed jets experiments.

The flow strength can be described by the Deborah number, D, which is the dimensionless strain rate given by the product of $\dot{\epsilon}\tau$. The Deborah number is scaled so that the critical strain rate, $\dot{\epsilon}_c$, corresponds to $D = 1$. The results of the simulations presented by Hinch are typically in the range of $W_c = 100 - 10^5$, where W_c is the chain Weissenberg number (approximately equivalent to Deborah number)[20]. In the opposed jets experiments, the Deborah numbers corresponding to the M_p of the polymer samples typically rise to $D = 3$–4 (although the Deborah numbers for the higher molecular weight components in the distribution will be larger). Thus, the flow regime in the opposed jets is not comparable with the flow fields of the kinks dynamics simulations. Note that the kinks dynamics simulations show that as the flow strength is reduced, so the proportion of chain segments involved in kinks reduces. Very strong flows are likely to have a significant effect on chain segments, because the segmental relaxation times are being approached. The question of whether high segmental orientation at relatively low molecular strains, and an

uncoiling mechanism following kinks dynamics, is applicable to the flow fields in the opposed jets apparatus, cannot be answered until simulations in the appropriate flow regime are considered.

RESULTS AND DISCUSSION

Flow field analysis

The potential flow calculation has been applied to the jet geometry used for the initial experiments ('glass jets' in ref. 1). The dimensions of these jets are $r_j = 0.175$ mm, $r_e = 0.875$ mm and $\delta = 0.285$ mm. The streamlines are shown in *Figure 3*. This plot presents only the region (r, $z > 0$), which due to the symmetry, contains all the required information.

The streamlines obtained for the case of uniaxial extension have also been calculated, and these are shown in *Figure 4*. (N.B. The geometry used to calculate this uniaxial extension plot is not the same as that given above. However, the streamlines for uniaxial extension are expected to be very similar, and *Figure 4* is given for comparison purposes). In the region far from the stagnation point, clear differences between the potential flow and the uniaxial extension can be seen, as would be expected. However, even in the region between the jets, it is evident that the streamline patterns in the calculated potential flow differ appreciably from the uniaxial extension case.

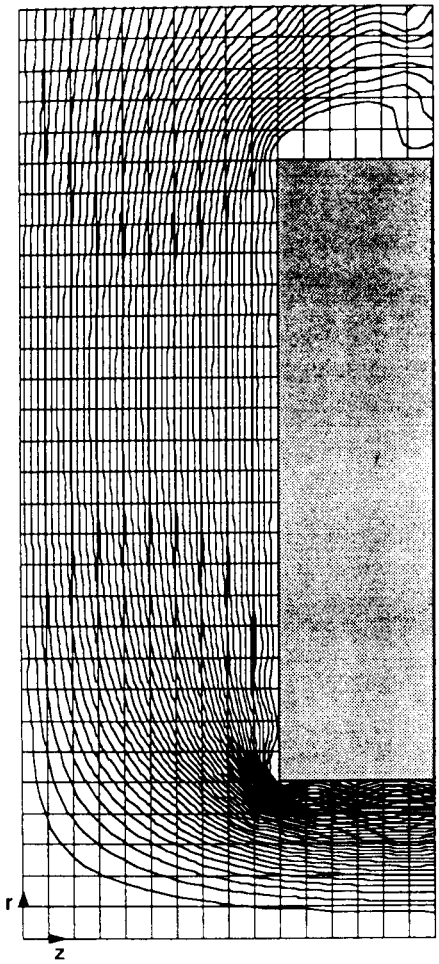

Figure 3 Streamlines calculated for the glass jets geometry (potential flow calculation)

A contour plot of $\dot{\epsilon}_{zz}$, the strain rate in the z-direction, in the region between the capillary walls ($0 < z < \delta$, $0 < r < r_j$) has also been generated (*Figure 5*). Previously, $\dot{\epsilon}_{zz}$ has necessarily been assumed to be constant throughout the region between the jets, with an approximate value given by the nominal strain rate, $\dot{\epsilon}_{nom}$. The contours are labelled with the value of the ratio between the real $\dot{\epsilon}_{zz}$ and $\dot{\epsilon}_{nom}$. The plot reveals that $\dot{\epsilon}_{nom}$ is not reached at the stagnation point (where the strain rate ($\dot{\epsilon}_o$) is only $0.493\,\dot{\epsilon}_{nom}$), and that $\dot{\epsilon}_{zz}$ varies dramatically across the region. Along the centre line, $r = 0$, the strain rate increases as the fluid element flows towards the capillary from the stagnation point, and then decreases when the fluid element approaches the capillary entrance. This indicates significant departures from uniaxial extension.

A detailed knowledge of the flow field, as provided by the simulations, yields the precise strain rate history to which the polymer molecules have been subjected, providing that the polymers are not significantly modifying the flow. This information allows the fluid strain accumulated at or above the critical strain rate to be calculated, for comparison with molecular strain.

The contour plot (*Figure 5*) shows a decrease in $\dot{\epsilon}_{zz}$ with radial distance, r, from the stagnation point. Therefore, an incoming molecule along the central streamline experiences an increasing strain rate as the stagnation point is approached, until at a particular r value (r_o), the strain rate becomes equal to $\dot{\epsilon}_c$, the critical strain rate. Molecular strain can begin to accumulate at this point, and therefore it is the starting point for the integration of the fluid strain.

The strain rate of a fluid element in the z-direction is defined as:

$$\dot{\epsilon}_{zz} = \dot{\epsilon} = \frac{1}{\ell}\frac{d\ell}{dt} = \frac{v_r}{\epsilon}\frac{d\epsilon}{dr} \tag{7}$$

where ℓ is the length of the fluid element in the z-direction, v_r is its radial velocity and ϵ is the fluid strain.

The flow field simulation yields $\dot{\epsilon}(r)$ and $v_r(r)$ on the symmetry plane, making it possible to separate variables and integrate equation (7)

$$\ln(\epsilon) = \int_{r_o}^{r} \frac{\dot{\epsilon}}{v_r} dr \tag{8}$$

Equation (8) gives the fluid strain accumulated between the points r_o and r.

Empirical equations have been fitted to the plots of $\dot{\epsilon}(r)$ and $v_r(r)$ generated by the simulation, in the vicinity of the stagnation point (*Figures 6* and *7*). The procedure for determining r_o at a given value of $\dot{\epsilon}_{nom}$ is thus simplified, with $\dot{\epsilon}(r)$ and $v_r(r)$ being substituted into the integration. The value of $\dot{\epsilon}_o$ is found by multiplying $\dot{\epsilon}_{nom}$ by 0.493.

The potential flow field for a second jet geometry ('metal jets' in ref. 1) has also been evaluated. The dimensions of these jets are $r_j = 0.3$ mm, $\delta = 0.175$ mm and $r_e = 1$ mm. The normalized $\dot{\epsilon}_{zz}$ contour map is shown in *Figure 8*. This flow field more closely resembles the ideal case, but the strain rate still changes appreciably in the region around the stagnation point, and is equal to $0.702\,\dot{\epsilon}_{nom}$ at the stagnation point.

The study of various different jet dimensions has shown that the parameter (r_j/δ) is the controlling factor

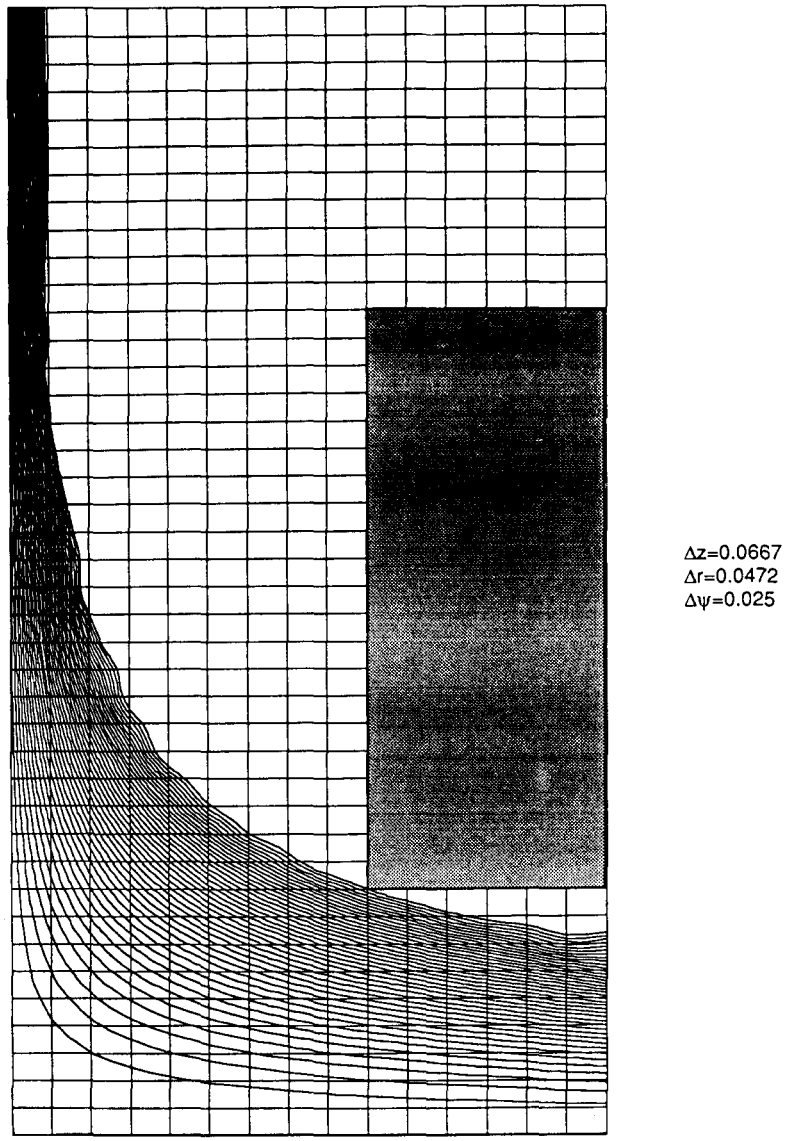

Figure 4 Streamlines calculated for pure uniaxial extension

in the pattern of the strain rate distribution. The higher the value of the ratio r_j/δ the closer the flow is to ideal uniaxial extension, however in practice, large ratios are difficult to achieve.

A comparison of the viscous flow simulation with the potential flow simulation, for the 'metal jets', reveals quantitative differences. However, the accumulated fluid strain predicted by the potential flow model is only slightly higher than that of the viscous model, except at very small r and very high strains (close to the stagnation point). In reality, the flow field would lie somewhere between the potential and viscous limits, but since these two extremes showed little difference, further investigation was not undertaken.

Molecular and fluid strain profiles

By using the assumption that the birefringence value at the plateau of the Δn_{max} vs. $\dot{\epsilon}$ curves corresponds to fully stretched molecules, it is possible to convert the birefringence to 'molecular strain' profiles. Such profiles can then be compared to the available fluid strains.

The samples used in this study contain a degree of polydispersity and therefore molecules of different molecular weight will stretch over a range of strain rates. Due to the low polydispersity of the samples used, it was possible to use an average value of $\dot{\epsilon}_c$ (corresponding to the central strain rate of the sigmoidal Δn_{max} vs. $\dot{\epsilon}$ curve), and a value of t_{max} calculated from the M_p value of the sample. (Note that t_{max} values for aPS samples were assessed using data obtained under θ-conditions[21].) The errors introduced, as a consequence of this choice, will be more significant at low strain rates, since a large proportion of the sample is still to be stretched. The problem of residual polydispersity is further discussed at appropriate points later in this section.

Strain profiles: glass jets geometry. The first strain analysis was applied to the 0.01% $M_p = 8 \times 10^6$ aPS/decalin solution, which was analysed in the 'glass jets', and the potential flow model was used to describe the flow field. *Figure 9* shows the fluid and molecular strains at several strain rates. Note that the birefringence profiles at the higher strain rates indicate that some degree of flow modification is present and therefore the actual fluid

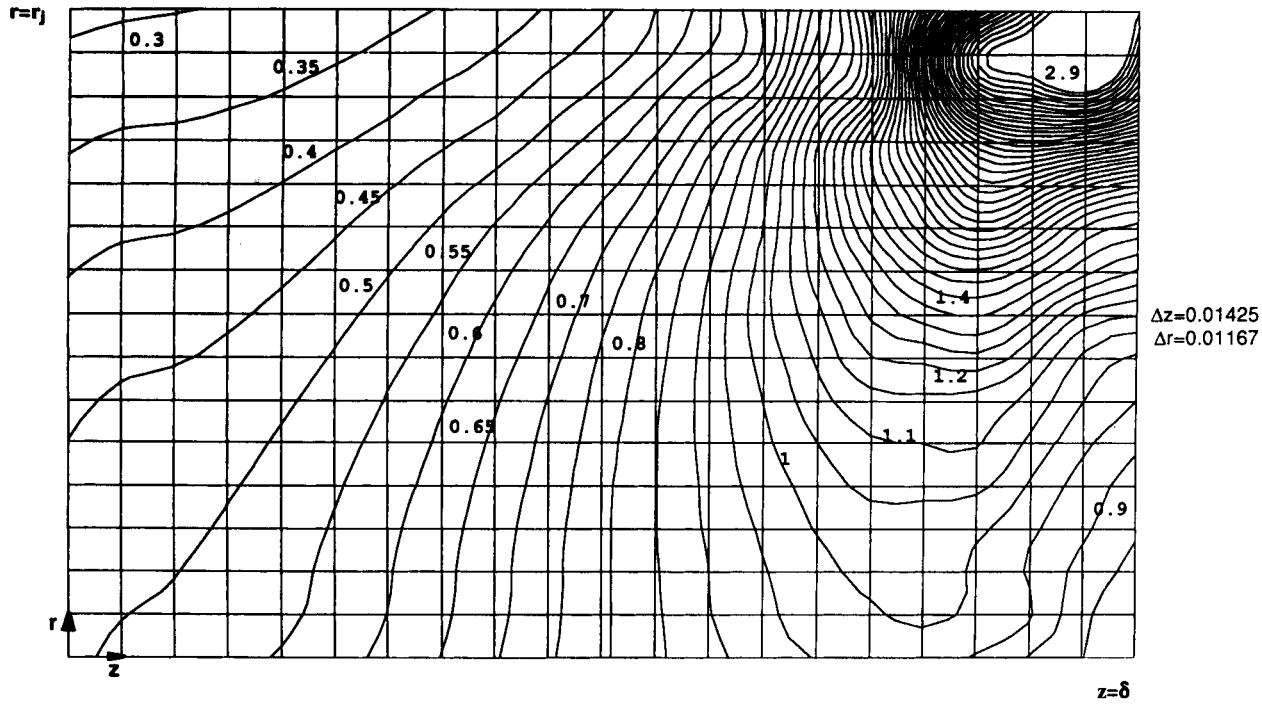

Figure 5 Contour plot of strain rate in the z-direction ($\dot{\epsilon}_{zz}$) in the region between the jets ($0 < z < \delta$, $0 < r < r_j$), for the glass jets geometry (potential flow calculation). The contours are labelled with the value of the ratio between the real $\dot{\epsilon}_{zz}$ and the nominal strain rate, $\dot{\epsilon}_{nom}$

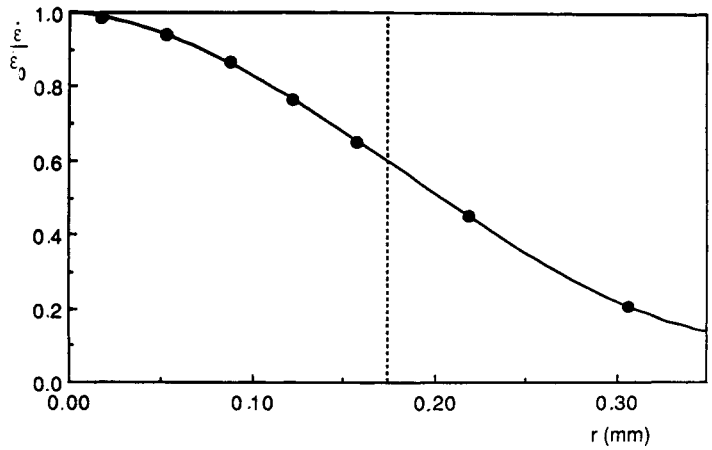

Figure 6 Normalized strain rates at $z = 0$ (glass jets geometry). Data points: potential flow simulation; curve: empirical fit to the data

strain profiles will differ from the calculated profiles[1]. The cut-off of molecular strain data at around 20 (log 1.3) corresponds to the limit of measurable retardation [$\approx\lambda/(3 \times 10^4)$].

Despite the unavailability of low molecular strain information, *Figure 9* clearly reveals that the initial deformation is *non-affine* with the fluid strain. At a nominal strain rate of $\dot{\epsilon}_{nom} = 6000\,s^{-1}$, the flow analysis shows that molecular strain should begin to accumulate at $r_o = 0.29$ mm (the point at which $\dot{\epsilon}$ becomes equal to $\dot{\epsilon}_c$). However at $r = 0.025$ mm, the molecular strain is more than 2 orders of magnitude smaller than the fluid strain accumulated since $r = r_o$. This demonstrates that a considerable degree of slip with respect to the fluid has taken place.

Note, however, that for r values in the range 0.02mm $\leqslant r \leqslant 0.025$ mm (for $\dot{\epsilon}_{nom} = 6000\,s^{-1}$), the fluid and molecular strain curves are parallel. The strain axis is a logarithmic scale and therefore parallel curves indicate an identical deformation rate with respect to r, i.e. the molecular deformation is affine with the fluid deformation over the given range of r. As $r \rightarrow 0$ (on approach to the stagnation point), the fluid strain tends to infinity, whereas the molecular strain must saturate at full extension. Thus, non-affine molecular deformation with respect to the fluid is an inevitable result.

The region of significant molecular extension can be seen to broaden as the strain rate increases. This effect partly arises from a higher available strain with increasing strain rate, but there is evidence to suggest a more affine mode of molecular deformation (i.e. there is less slip with respect to the fluid) at higher strain rates. The ratio of fluid strain, ϵ, to molecular strain, t, at a given value of t, can be calculated for different strain rates, to obtain a parameter which characterizes the degree of affinity. At $\log(t) = 1.5$, for example, $\epsilon/t \approx 500$ at $\dot{\epsilon}_{nom} = 2500\,s^{-1}$, whereas $\epsilon/t \approx 210$ at $\dot{\epsilon}_{nom} = 6000\,s^{-1}$.

The molecular and fluid strains have been plotted as a

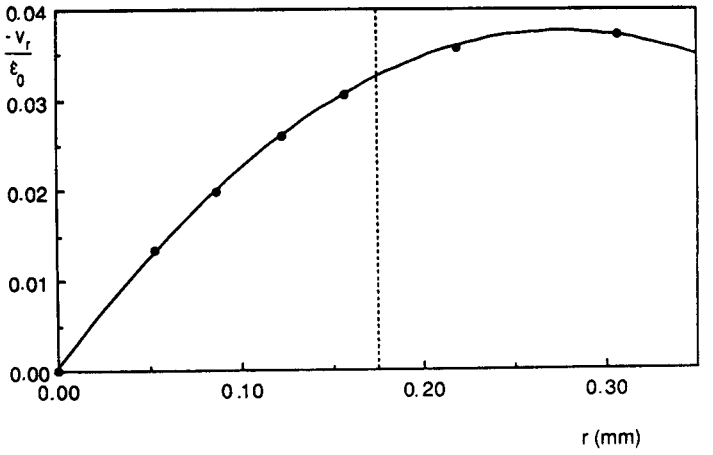

Figure 7 Normalized radial velocity at $z = 0$ (glass jets geometry). Data points: potential flow simulation; curve: empirical fit to the data

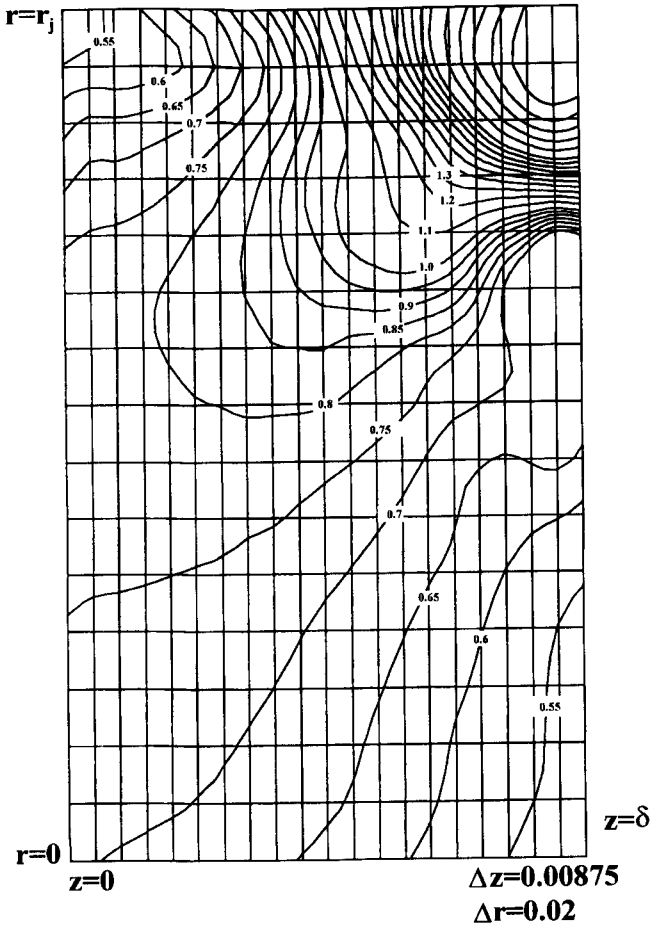

Figure 8 Contour plot of strain rate in the z-direction ($\dot{\epsilon}_{zz}$) in the region between the jets ($0 < z < \delta$, $0 < r < r_j$), for the metal jets geometry (potential flow calculation). The contours are labelled with the value of the ratio between the real $\dot{\epsilon}_{zz}$ and the nominal strain rate, $\dot{\epsilon}_{nom}$

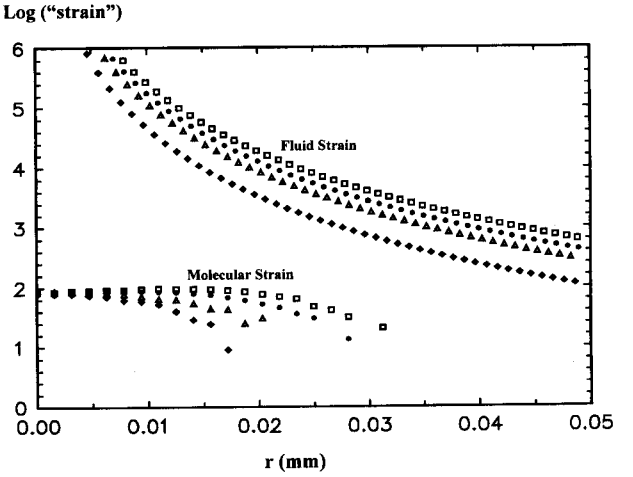

Figure 9 Molecular and fluid strains plotted against r for a 0.01% $M_p = 8 \times 10^6$ aPS/decalin solution, over a range of nominal strain rates (glass jets geometry). ◆, 2500 s^{-1}; △, 4000 s^{-1}; ●, 6000 s^{-1}; □, 12000 s^{-1}

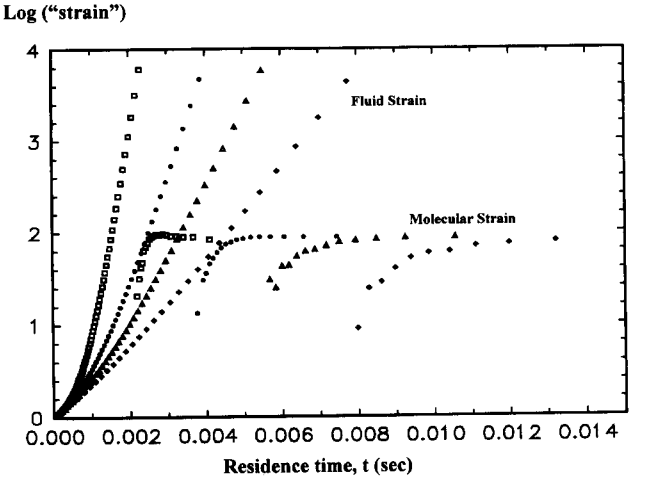

Figure 10 Molecular and fluid strains plotted against residence time (t) for a 0.01% $M_p = 8 \times 10^6$ aPS/decalin solution, over a range of nominal strain rates (glass jets geometry). ◆, 2500 s^{-1}; △, 4000 s^{-1}; ●, 6000 s^{-1}; □, 12000 s^{-1}

function of r, but it is also possible to create plots of strain as a function of residence time. *Figure 10* is a plot of residence time *versus* log strain for several different strain rates. Taking the data for $\dot{\epsilon}_{nom} = 6000\,s^{-1}$ as an example, it can be seen that the fluid and molecular strain curves are approximately parallel at the lowest molecular strains detectable, indicating an equal rate of deformation before saturation of the molecular strain occurs.

(Note that the molecular strain curves sometimes appear to be steeper than the fluid strain curves in the low strain region, which is obviously a physically unrealistic situation. The origin of this effect is discussed later in the section.) The vertical separation of the two strain curves points to non-affine deformation at the beginning of molecular uncoiling. As previously stated, low molecular strain data are unavailable, but at $t_{res} = 0$, the fluid and molecular strain curves must coincide by definition. The consequence of this is that the form of the molecular strain curve must be sigmoidal, which is consistent with a change in draining properties on extension. The longest conformational relaxation time of the molecule can be described as the ratio of the hydrodynamic friction coefficient (f) and the entropic elastic restoring force coefficient (k), where both f and k are functions of molecular extension ratio (β)[22]. At low β, changes in f are most significant; solvent penetration into the coil interior is increased as more of the coil is exposed, producing a higher f value. This results in an increased τ and a reduced $\dot{\epsilon}_c$. At constant $\dot{\epsilon}$, there is a rapid transition from the coiled to the stretched state, and affine deformation would be possible. It is likely that significant changes in the value of f would only occur after a certain initial degree of uncoiling.

Figure 10 also shows that as the strain rate increases, the onset of affine deformation is seen to occur at lower residence times in the flow field, but a finite delay remains evident.

Strain profiles: metal jets geometry. The strain analysis was applied to data in the metal jets for which flow modification appeared to be minimal. The potential flow model was used to describe the flow field since inertial effects are significant[11,12]. In reality, the flow field would lie somewhere between the viscous and potential limits. The fluid strains predicted by the potential flow simulation have been found to be generally slightly higher than those predicted by the viscous flow simulation, except at very small r (close to the stagnation point).

Figure 11 shows the molecular and fluid strains at two different strain rates for a 0.01% $M_p = 8.5 \times 10^6$ aPS/decalin solution, and reveals that the molecular deformation is much more affine with the fluid strain. In fact, the application of the selected birefringence–molecular strain relationship for this molecular weight appears to show that the molecular deformation is perfectly affine with the fluid strain (note that the lowest molecular strain values are subject to the highest signal-to-noise ratio). The molecular strain only becomes non-affine with the fluid when saturation occurs at full molecular extension. This picture is in marked contrast to the results from the potential flow simulation in the glass jets, where the molecular strain was shown to be approximately 2 orders of magnitude smaller than the fluid strain, prior to molecular strain saturation (*Figure 9*). Note that at a comparable r value, the fluid strain in the glass jets is much higher than in the metal jets, and that the width of the region of high molecular extension in the metal jets is greater than that in the glass jets.

Figure 12 shows the molecular and fluid strains at two different strain rates for a 0.01% $M_p = 4 \times 10^6$ aPS/decalin solution. Much more affine molecular deformation with the fluid is again indicated, with the initial molecular strain curves running slightly below, but parallel to the fluid strain curves. The t_{max} value has been reduced from that in *Figure 11* because of the lower molecular weight sample used. *Figure 12* provides evidence that the molecular deformation becomes more affine as the strain rate increases. At $\log(t) = 1.5$, $\epsilon/t \approx 20$ at $\dot{\epsilon}_{nom} = 11\,000\,s^{-1}$, whereas $\epsilon/t \approx 1.5$ at $\dot{\epsilon}_{nom} = 25\,500\,s^{-1}$. (Note that ϵ/t ratios in the glass jets were of the order of 10^2.)

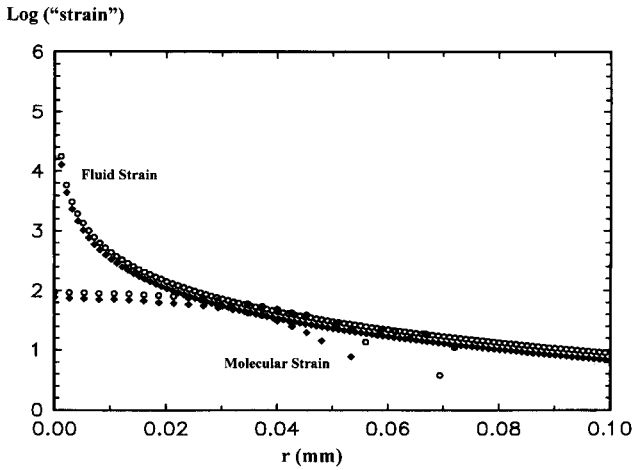

Figure 11 Molecular and fluid strains plotted against r for a 0.01% $M_p = 8.5 \times 10^6$ aPS/decalin solution, at a nominal strain rate just above $\dot{\epsilon}_c$ (◆, $4350\,s^{-1}$) and at a nominal strain rate which shows the maximum experimental (plateau) birefringence (○, $15\,900\,s^{-1}$) (metal jets geometry)

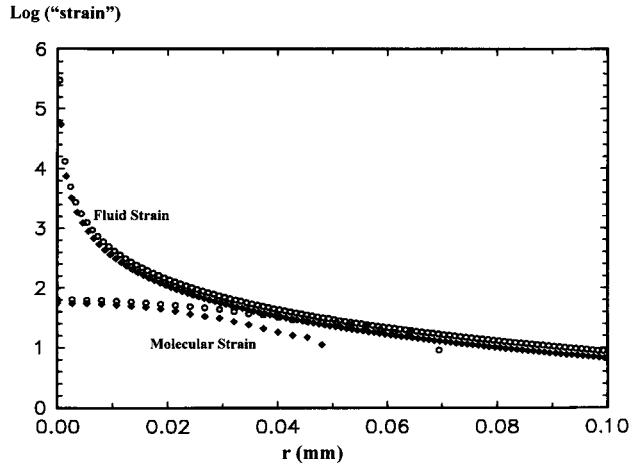

Figure 12 Molecular and fluid strains plotted against r for a 0.01% $M_p = 4 \times 10^6$ aPS/decalin solution, at a nominal strain rate just above $\dot{\epsilon}_c$ (◆, $11\,000\,s^{-1}$) and at a nominal strain rate which shows the maximum experimental (plateau) birefringence (○, $25\,500\,s^{-1}$) (metal jets geometry)

Figure 13 shows plots of residence time vs. log strain at two different strain rates, for a 0.01% $M_p = 4 \times 10^6$ aPS/decalin solution. For this molecular weight sample at the lower strain rate, there is some vertical separation between the molecular strain and fluid strain curves at the onset of molecular uncoiling, which points to a finite delay before affine deformation occurs. As the strain rate increases, the vertical separation between the molecular and fluid strain curves reduces, and a mode of affine deformation is seen to initiate at lower residence times in the flow field. In fact at $\dot{\epsilon}_{nom} = 25\,500\,s^{-1}$, the fluid and molecular strain curves appear to superimpose at low molecular strains, suggesting affine deformation (using the given birefringence–molecular strain relationship).

The viscous flow simulation for the metal jets geometry was used to describe the flow field in the case of the 0.005% $M_p = 8.5 \times 10^6$ aPS/TCP solution. *Figure 14* shows the molecules and fluid strains at $\dot{\epsilon}_{nom} = 240\,s^{-1}$, as a function of r. The plot reveals that the molecular strain is apparently greater than the fluid strain from the start of molecular uncoiling. This is obviously unrealistic. Two factors are contributory to this observation. Firstly, the calculated fluid strain is not entirely valid due to severe modification of the flow field[1]. The localized regions of high extensional viscosity cause screening of the flow field about the central axis, which may force the stagnation point outwards, and create a stagnation surface (this picture is equivalent to flow around a solid cylinder, and therefore a simple shear component in the flow field would be introduced at the surface of the cylinder). As a consequence, r_o may also be moved outwards, and therefore the calculated fluid strain at a given r is likely to be lower than the actual fluid strain. Secondly, the overestimation of t_{max} due to non-θ-conditions of aPS/TCP at 23°C (expansion parameters for aPS in TCP are unknown) generates a calculated molecular strain which is higher than the actual molecular strain.

For another good solvent system, 0.02% $M_p = 1.39 \times 10^6$ PEO/water, there appeared to be no signs of flow modification. The potential flow model has been used to describe the flow field due to the low viscosity of water. *Figure 15* shows the molecular and fluid strains at $\dot{\epsilon}_{nom} = 35\,050\,s^{-1}$. The molecular deformation is apparently affine with the fluid. *Figure 16* is a strain vs. residence time plot for the same strain rate. As would be expected, there is no vertical separation between the fluid and molecular strain curves at low molecular strains. In contrast to the aPS/TCP solution, we do not now observe anomalous apparent molecular strains that are substantially higher than the available fluid strains, supporting the hypotheses that the irregularity with aPS/TCP arises largely from flow modification. In the case of PEO/water, the value for t_{max} is expected to be valid, due to the use of data obtained under non-θ-conditions[21].

The effect of solvent quality. The results obtained for an aPS/decalin solution can be compared with an aPS/TCP solution, using the same molecular weight polymer in the metal jets. The viscous flow simulation is appropriate

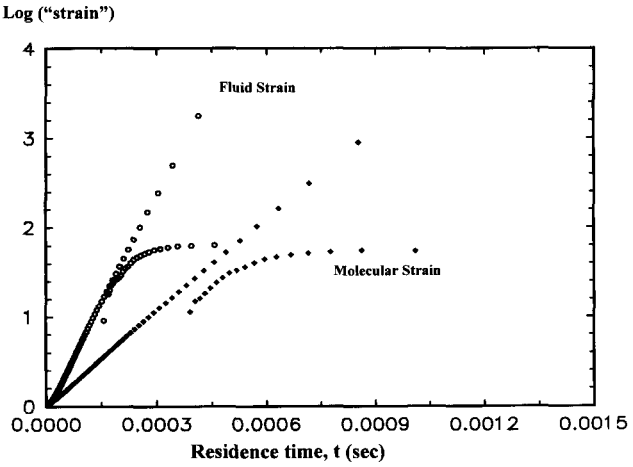

Figure 13 Molecular and fluid strains plotted against residence time (t) for a 0.01% $M_p = 4 \times 10^6$ aPS/decalin solution, at a nominal strain rate just above $\dot{\epsilon}_c$ (◆, $11\,000\,s^{-1}$) and at a nominal strain rate which shows the maximum experimental (plateau) birefringence (○, $25\,500\,s^{-1}$) (metal jets geometry)

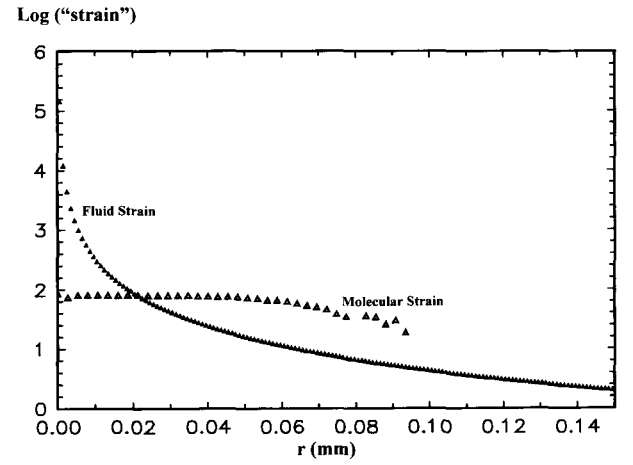

Figure 14 Molecular and fluid strains plotted against r for a 0.005% $M_p = 8.5 \times 10^6$ aPS/TCP solution, at a nominal strain rate of $240\,s^{-1}$ (metal jets geometry)

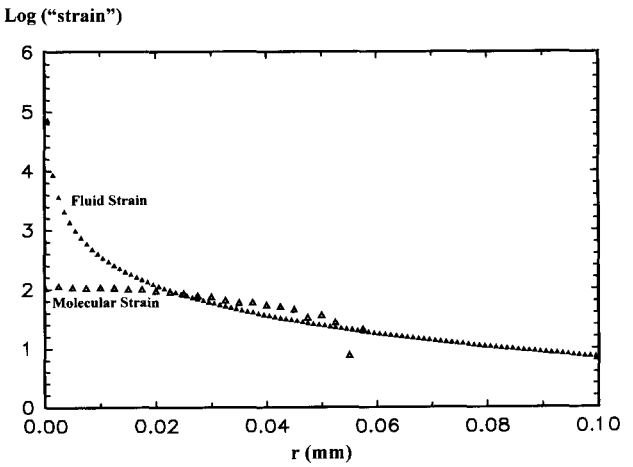

Figure 15 Molecular and fluid strains plotted against r for a 0.02% $M_p = 1.39 \times 10^6$ PEO/water solution, at a nominal strain rate of $35\,050\,s^{-1}$ (metal jets geometry)

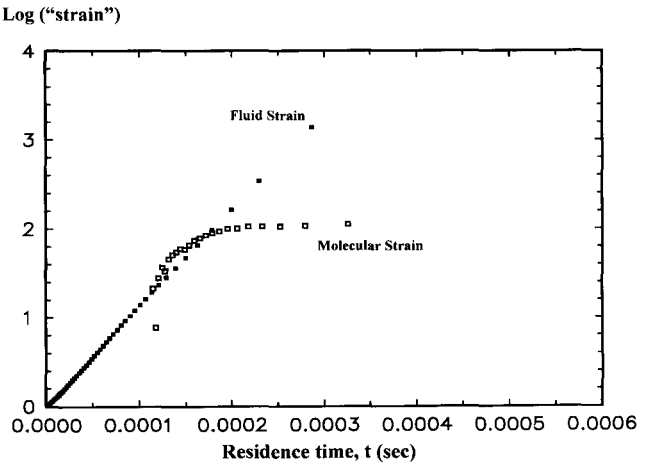

Figure 16 Molecular and fluid strains plotted against residence time (t) for a 0.02% $M_p = 1.39 \times 10^6$ PEO/water solution, at a nominal strain rate of $35\,050\,s^{-1}$ (metal jets geometry)

for TCP, but the actual flow field for decalin is likely to be intermediate between the viscous and potential limits (although the accumulated strain profiles only differ a little in the two models).

The experimental results show that the region of high molecular extension for a 0.005% $M_p = 8.5 \times 10^6$ aPS/TCP solution is significantly broader than the comparable region for a 0.01% $M_p = 8.5 \times 10^6$ aPS/decalin solution (*Figures 14* and *11* respectively).

The molecular relaxation time is predicted to scale with solvent viscosity[6], and therefore $\dot{\epsilon}_c$ should be reduced accordingly in a higher viscosity solvent. The viscosity of TCP is ≈20 times that of decalin at room temperature. Due to the severe flow screening present in the aPS/TCP solution[1], it is difficult to obtain a value of $\dot{\epsilon}_c$ for the M_p of the molecular weight distribution from the Δn_{max} vs. $\dot{\epsilon}$ curve, which could then be compared with the $\dot{\epsilon}_c$ for the decalin solution. However, the onset strain rate at which a birefringent signal was first detected should provide information about scaling between the two solutions (although the TCP profiles show apparent flow modification even at the initial strain rates, which may influence the shape of the Δn_{max} vs. $\dot{\epsilon}$ curve[1]). The strain rate at which a birefringent signal is first detected for the 0.01% $M_p = 8.5 \times 10^6$ aPS/decalin solution is $720\,s^{-1}$. Allowing for concentration and extrapolating the initial part of the Δn_{max} vs. $\dot{\epsilon}$ curve provides an equivalent onset strain rate for the 0.005% $M_p = 8.5 \times 10^6$ aPS/TCP solution of approximately $28\,s^{-1}$. The ratio of these strain rates is ≈26, which is rather greater than the scaling between the two solvent viscosities. This difference may be accredited to the change in solvent quality.

At a temperature of 23°C (experimental conditions), decalin is expected to be close to a θ-solvent for aPS, and TCP is expected to be a good solvent. The initial molecular conformation of aPS (prior to any perturbation by flow) will be more expanded in TCP than in decalin, which reduces the value of t_{max} (for a given molecular weight species), and the deformation should be more affine with the fluid, due to reduced hydrodynamic interaction in the more expanded coil. The outcome would be a broader region of high molecular extension in a good solvent, as compared to a θ-solvent, and a corresponding increase in the perturbation of the flow field.

The system of PEO in water is of relatively low viscosity, which is comparable with the aPS/decalin solutions. However, water is a good solvent for PEO, and on this basis is comparable to the highly viscous aPS/TCP system. The experimentally derived molecular strain profiles for PEO/water are essentially showing a highly affine mode of deformation with the fluid. This is in qualitative agreement with the experimental results for aPS/TCP.

A comparison of molecular behaviour can be made between the two good solvent systems, i.e. PEO/water and aPS/TCP. The region of significant molecular extension has been found to be greater for $M_p = 8.5 \times 10^6$ aPS/TCP (*Figure 14*), as compared to $M_p = 1.39 \times 10^6$ PEO/water (*Figure 15*). This is due to the PEO sample having a higher t_{max} value than the aPS sample, and thus PEO requires more accumulated strain to become fully extended. The contour length of the aPS molecule is greater than that of the PEO molecule, and therefore would be expected to create a higher extensional viscosity. This change in molecular parameters explains why severe flow modification occurs for the aPS/TCP system, but is apparently absent for PEO/water.

The effect of chain flexibility. Tatham *et al.* have studied the molecular behaviour of hydroxypropyl guar (HPG), in the glass jets geometry[23]. HPG is an inherently less flexible molecule than either aPS or PEO, but maintains a coil-like structure (rather than being a completely rigid rod). The retardation and birefringence profiles for HPG/water solutions are found to be much broader than those for aPS, since less strain is required for HPG to attain full extension. The HPG also appears to stretch more affinely with the fluid at the start of the uncoiling process. This is consistent with predictions for a more expanded molecule, which has a less significant change in draining characteristics on extension than would be the case for a highly flexible molecular coil with strong hydrodynamic screening.

Factors affecting the derived molecular strain profiles

The analysis of the molecular strain profiles has revealed certain problems with the chosen procedure. The first of these is that, in some cases, the molecular strain is apparently greater than the fluid strain, e.g. *Figure 14*. The second problem appears at low molecular strains, where the gradient of the molecular strain vs. r curve is often seen to be greater than that of the corresponding fluid strain curve, e.g. *Figure 11*. This implies that the molecular strain is accumulating more rapidly than the available fluid strain (although the data points at low molecular strains are subject to the highest noise). The following factors may contribute to the above discrepancies.

Due to the uncertainty in the theoretical value of the birefringence of fully stretched polystyrene molecules in solution[1,12] the value of Δn_o in the molecular strain analysis has been taken as the maximum experimental birefringence, i.e. the plateau value of Δn_{max}. This effectively fixes the value of maximum molecular strain, and the molecule is assumed to be fully stretched. However, as shown previously, the magnitude of the maximum experimental birefringence is an increasing function of molecular weight[1,12]. This has been interpreted as an increased proportion of the molecule being involved in a relatively unstretched end-region for lower molecular weights. The consequence of taking the plateau value of Δn_{max} to be Δn_o in the molecular strain analysis would therefore be an overestimate of molecular strain for lower molecular weight samples.

The effect of changing Δn_o may be studied by re-analysing the molecular strain data for the 0.01% aPS/decalin solutions of $M_p = 4 \times 10^6$ and $M_p = 3 \times 10^6$ (in the metal jets), using the Δn_{max} value of 0.01% $M_p = 8.5 \times 10^6$ aPS/decalin as Δn_o, such that the overestimate in molecular strain for the lower molecular weight samples would be reduced. The outcome of the change in Δn_o is that the molecular strains are reduced, but the gradient of the molecular strain vs. r curve, at low molecular strains, still appears to be greater than that of the fluid strain curve.

The choice of a birefringence–molecular strain relationship which is inappropriate for molecular uncoiling in the flow field in question, would be an obvious factor causing apparent anomalies in the derived molecular strain profiles. In the discussion of the uncoiling process

proposed by Treloar, it has been stated that the results are likely to be an overestimate. The kinks dynamics simulations of chain unravelling in extensional flows can produce birefringence values which are close to Δn_0 for comparatively low molecular strains[19,20]. However, as discussed previously, such simulations are in an inappropriate flow regime.

The Treloar model of chain uncoiling provides an explicit, monotonically increasing relationship between birefringence and molecular strain. On this basis, the model is a fair starting point for molecular strain derivation in an extensional flow field created by the opposed jets. The model corresponds to a stretching force applied only at chain ends. The neglect of the forces generated by streaming solvent along the chain may lead to an overestimate of t, which would be most significant at low t values. The unavailability of theoretical predictions, in comparable flow regimes to the experiments, means that an alternative model cannot be readily applied.

Theoretical simulation of molecular behaviour

A theoretical model for the polymer chain has been subjected to the flow field simulations obtained for the opposed jets, and the subsequent molecular deformation has been monitored.

The model chosen to simulate the deformation of a polymer molecule in an extensional flow field was the FENE dumb-bell model of Hinch and Harlen *et al.*, which incorporates non-linear friction on extension[24,25]. The evolution of the dimensionless dumb-bell extension, R, with time, t, is given by

$$\frac{dR}{dt} = R\frac{\partial v_z}{\partial z} - \frac{4(R-1)}{DR[1-(R^2/L^2)]} \qquad (9)$$

where D is the Deborah number (scaled so that $\dot{\epsilon}_c$ corresponds to $D = 1$), and L is the extensibility of the dumb-bell. The first term on the right-hand side of equation (9) corresponds to affine deformation, and a 'slip' term is subtracted from this.

A computer program integrates the above equation as the molecule approaches the stagnation point. The program follows a fluid element from a distance 0.3 mm away from the stagnation point. Using the flow field analyses of the opposed jets, the local strain rate is calculated, along with the accumulated strain. Over a constant time interval (0.001 s), dR/dt and the radial velocity are determined, which then allows a new position for the next time interval to be calculated. The increment dR is added to R, and the above process is repeated. The simulation stops 0.5 μm away from the stagnation point.

The 'slip' term in equation (9) can be scaled by a factor (χ) of between 0 and 1, which varies the degree of affinity. For $\chi = 0$, there is no slip with respect to the fluid (and the finite extensibility of the dumb-bell is removed), and therefore this analysis gives an estimation of the accumulated fluid strain.

Theoretical predictions of molecular deformation have been applied to the potential flow simulation of the glass jets, and the potential and viscous flow simulations of the metal jets. The molecular weight used in the FENE dumb-bell simulations was equivalent to the M_p of the molecular weight distribution of the aPS samples used experimentally. *Figure 17* shows the molecular strain vs. r profiles obtained from the FENE simulation for a polymer of molecular weight 8×10^6 at various Deborah numbers, in the potential flow field of the glass jets, together with the fluid strain. *Figure 18* presents comparable data for a molecular weight of 8.5×10^6 in the potential flow field of the metal jets (note that the simulations of the potential and viscous flows in the metal jets are very similar).

Generally, the FENE simulations reveal that as the flow strength (Deborah number) is increased, the molecular deformation becomes more affine with the fluid, and the width of the high molecular strain region increases. This is in accordance with the experimental results.

Observation of birefringence and related Deborah numbers. The FENE simulations show that for a given Deborah number, the width of the region of significant molecular strain in the glass jets should be greater than the comparable region in the metal jets. This situation is not found in the molecular strain profiles derived from the experimental results, which show a broader region of significant molecular extension in the metal

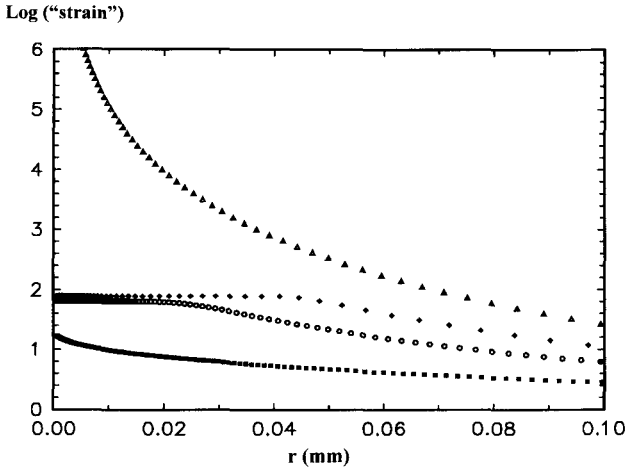

Figure 17 Molecular and fluid strain profiles plotted against r, from the non-linear hydrodynamic friction FENE dumb-bell simulation for a polymer of molecular weight 8×10^6 in the potential flow field of the glass jets. ■, Molecular strain at $D = 1$; ○, molecular strain at $D = 2$; ◆, molecular strain at $D = 4$; ▲, fluid strain

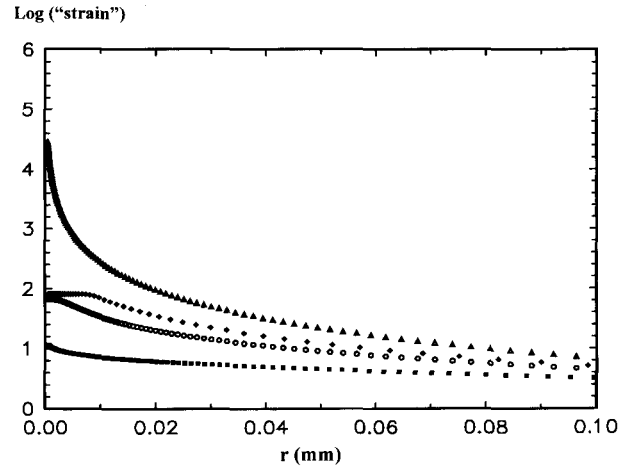

Figure 18 Molecular and fluid strain profiles plotted against r, from the non-linear hydrodynamic friction FENE dumb-bell simulation for a polymer of molecular weight 8.5×10^6 in the potential flow field of the metal jets. ■, Molecular strain at $D = 1$; ○, molecular strain at $D = 2$; ◆, molecular strain at $D = 4$; ▲, fluid strain

jets, as compared to the glass jets (*Figures 9* and *11*). The simulations predict a narrow region of high molecular extension in the metal jets, which implies that when the birefringent signal is first detected experimentally, the Deborah number is likely to be significantly higher than 1. At a strain rate for which the Δn_{max} vs. $\dot{\epsilon}$ curve has saturated, all of the molecular weight distribution would be subject to a flow strength of at least $D = 1$ (and would therefore be highly extended), but a large proportion of the distribution would be experiencing a flow strength significantly higher than $D = 1$.

In the glass jets, the simulations predict a broader region of high molecular extension than in the metal jets, which implies that at the point of initial experimental detection, the Deborah number would be much closer to 1, i.e. the birefringent signal would be first detected at a lower flow strength in the glass jets, as compared to the metal jets. The 0.01% $M_p = 8 \times 10^6$ aPS/decalin solution in the glass jets shows evidence of significant flow modification, and it is likely that the Δn_{max} vs. $\dot{\epsilon}$ curve does not show a true saturation level for the whole molecular weight distribution[1,12]. Therefore, the full distribution may not be fully stretched and for the proportion that would be stretched, the flow strength would be likely to be $D = 1$ or just above. The simulated data for $D = 2$ provides a reasonable fit for the experimental data, showing that the width of the region of high molecular stretching and the displacement between the fluid and molecular strain curves are comparable. Equation (9) leads to a prediction of non-affine deformation for low Deborah numbers in the glass jets.

Note that for the glass jets geometry, only a potential flow simulation was available. For the metal jets geometry, the potential and viscous flow simulations revealed little difference in the accumulated fluid strains. The viscous simulation showed rather higher fluid strains for very small r. This would make very little difference to the evolution of macromolecular strain, which has saturated well before this point. For decalin solutions, the actual flow field is likely to move from the viscous regime towards the potential regime. A viscous simulation for the glass jets geometry may show a higher degree of affinity between the fluid and molecular strains.

The effect of polydispersity. The FENE simulations of the molecular strain profiles in the metal jets can be brought closer into line with the molecular strain profiles derived from experimental results, by considering polydispersity. The FENE simulations consider only a single molecular weight species, equivalent to the M_p of the molecular weight distribution of the sample used experimentally. At a flow strength of $D = 1$ for the M_p of the sample distribution, the higher molecular weight species would be experiencing a flow strength of $D > 1$, and therefore would deform more affinely with the fluid. Thus, the molecular strain profiles derived from the experimental results would be expected to show broader regions of high molecular extension, than FENE simulations performed with a monodisperse species. The effect of polydispersity on the molecular strain profiles obtained from the FENE simulations may be ascertained by the use of a model molecular weight distribution in the computational analysis, rather than a single molecular weight species.

The effect of solvent quality. The effect of solvent quality can be introduced into the non-linear hydrodynamic friction FENE dumb-bell model, by reducing the amount of slip between the molecule and the fluid. This may be done, somewhat arbitrarily, by scaling the 'slip' term by a factor (χ) of less than 1. *Figure 19* presents plots of molecular strain vs. r obtained from the FENE simulation for a polymer of molecular weight 8.5×10^6 at $D = 2$, in the viscous flow field of the metal jets, with varying degrees of slip (to account for a change in solvent quality). The molecular strain profile with $\chi = 0.3$ (arbitrarily chosen to approximate to a good solvent) can be seen to generate a broader region of significant molecular extension, and deform more affinely with the fluid, than the molecular strain profile with $\chi = 1$ (approximating to a θ-solvent).

Extensional viscosity increase due to molecular stretching

As previously shown, estimates of the increase in extensional viscosity due to molecular stretching are of the order of the number of flexible units in the chain (N), if the effective intrinsic extensional viscosity ($[\eta'_e]$) is corrected by a width parameter from the birefringence profiles[1]. For a 0.02% $M_p = 8 \times 10^6$ aPS/decalin solution, an estimate of the normalized extensional viscosity (H) was found to be 1390, with N for this sample being approximately 8000. A more realistic correction for the area of significant molecular extension may be obtained using the molecular strain profiles generated here. A relationship for extensional viscosity, η_e, as a function of molecular extension, t (or time), at constant strain rate, would enable an appropriate mean value of r (for the area correction) to be calculated. However, theoretical approaches do not appear to provide this explicit relationship, e.g. Bird *et al.* state that their treatment of the FENE dumb-bell model only provides expressions for the *steady-state* extensional viscosity as a function of strain rate[26].

An assumption has therefore been made that η_e varies as some power, x, of t. The exponent, x, is likely to assume a value at least as large as the power law dependence between the limiting value of the normalized

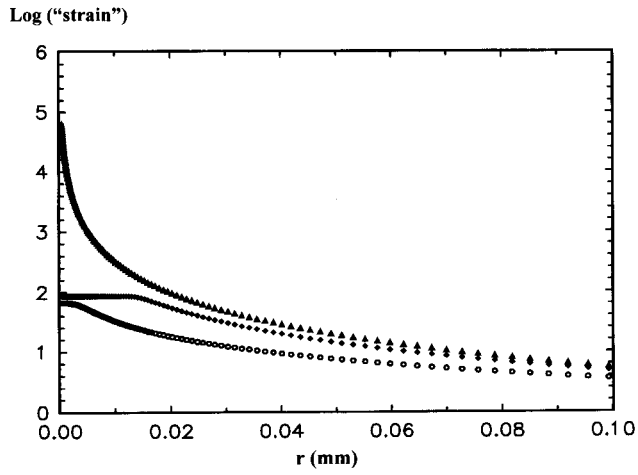

Figure 19 Molecular and fluid strain profiles plotted against r, from the non-linear hydrodynamic friction FENE dumb-bell simulation for a polymer of molecular weight 8.5×10^6 in the viscous flow field of the metal jets, with varying degrees of slip (to approximate a change in solvent quality). The Deborah number of the simulations is 2. ○, $\chi = 1$ (approximating to a θ-solvent; ◆, $\chi = 3$ (approximating to a good solvent); ▲, fluid strain

extensional viscosity, H, and the number of equivalent flexible units, N. Predictions of H have been shown to scale as N to N^3. Therefore, values of x of between 1 and 3 have been used to calculate the expectation value of r, $\langle r \rangle$, using the molecular strain profiles, $t(r)$, as follows:

$$\langle r \rangle = \frac{\sum r_i \cdot t_i^x}{\sum t_i^x} \tag{10}$$

The scaling of $[\eta_e']$ is now undertaken using $\langle r \rangle$. For values of x between 1 and 3, the values of H for aPS sample detailed above lie between 2300–3400. The results obtained do not depend very strongly on the value of x chosen. The increase in extensional viscosity due to stretched molecules is thus of the order of N.

Tatham has derived molecular strain profiles for hydroxypropyl guar (HPG), which is regarded as a worm-like molecule and is inherently less flexible than aPS[11]. Using the same approach as above to determine $\langle r \rangle$, the value of H was found to lie between 75–360 ($N_{HPG} \approx 100$).

CONCLUSIONS

The flow field simulations of the opposed jet geometries used experimentally, in the potential and viscous flow limits, enable the accumulated fluid strain to be calculated from the point at which the critical strain rate was attained. The flow simulations also permit the conversion of radial distance into residence time in the stretching flow. It has previously been assumed that the strain rate in the region between the jets was uniform, but the flow field simulations show that this is not the case. Strain rate distributions around the stagnation point depend strongly on jet geometry, which indicates that interpretation of these stretching flows requires a detailed strain history that can only be obtained from flow simulations. Uniaxial extension can be approached if the ratio of the jet diameter to the jet separation is large. Macromolecules can significantly modify the flow field, even at very low concentrations. Under such circumstances, the simulations of the flow fields would not provide valid fluid strains. The systems used in the present work are sufficiently dilute that flow modification is minimal.

We have attempted to compare the evolution of molecular strain with the available fluid strain. Treloar's model has been chosen to describe the process of macromolecular uncoiling, and provides a method for converting birefringence profiles to molecular strain profiles. In comparison to other models, this approach is likely to produce an overestimate of molecular strain, and therefore defines an upper bound for molecular strain.

The overall picture of molecular uncoiling in a uniaxial extensional flow field is one of non-affine deformation at the beginning of the process, consistent with changes in hydrodynamic interaction as the molecule extends. The results from two different jet geometries have been reconciled by performing simulations of molecular deformation, using the non-linear hydrodynamic friction FENE dumb-bell model. The experimental results show that changing from a θ-solvent to a good solvent causes a more affine mode of deformation, with a much wider region of significant molecular extension. For a high molecular weight polymer in a good solvent this can, in part, be due to severe flow modification. The effect of solvent quality can be introduced into the non-linear hydrodynamic friction FENE simulation, somewhat arbitrarily, by scaling the 'slip' term with a factor of between 0 and 1. The simulation for a good solvent shows an increase in the width of the region of significant molecular stretching, in agreement with the experimental results.

Effective intrinsic extensional viscosity values need to be corrected to take into account the area of significant molecular extension. The derivation of molecular strain profiles allows a correction to be made for the appropriate area, and therefore provides a more realistic assessment of the increase in extensional viscosity due to stretched molecules. The limiting values of this increase have been found to be of the order of the number of equivalent flexible units in the chain (N). This is consistent with the predictions of some simulations, but very much lower than the N^3 dependence predicted by others.

ACKNOWLEDGEMENTS

We gratefully acknowledge the financial support of BP Venture Research, EPSRC and the EU International Co-operation Programme. We are grateful for many useful discussions with Prof. A. J. Müller.

REFERENCES

1. Carrington, S. P., Tatham, J. P., Sáez, A. E. and Odell, J. A., *Polymer*, 1997, **38**, 4151.
2. Odell, J. A., Keller, A. and Müller, A. J., *Polymers in Aqueous Media*, ed. J. E. Glass, *Advances in Chemistry* 1989, **223**, 193.
3. Riande, E., Markovitz, H., Plazek, D. J. and Raghupathi, N., *J. Polym. Sci.: Symposium No. 50*, 1975, 405.
4. Bailey, F. E. Jr and Koleske, J. V., *Poly(ethylene oxide)*. Academic Press, New York, 1976.
5. Pope, D. P. and Keller, A., *Colloid and Polymer Sci.*, 1978, **255**, 633.
6. Keller, A. and Odell, J. A., *Colloid and Polymer Sci.*, 1985, **263**, 181.
7. Mackley, M. R., Ph.D. thesis, University of Bristol, 1972.
8. Schunk, P. R., de Santos, J. M., Macosko, C. W. and Scriven, L. E., *Proc. Xth Int. Congr. Rheol.* Sydney, 1988, p. 254.
9. Mikkelsen, K. J., Macosko, C. W. and Fuller, G. G., *Proc. Xth Int. Congr. Rheol.* Sydney, 1988, **2**, 125.
10. Bird, R. B., Armstrong, R. C. and Hassager, O., *Dynamics of Polymeric Liquids*, Vol. 1. John Wiley & Sons Inc., New York, 1977.
11. Tatham, J. P., Extensional flow dynamics of macromolecules of different flexibility in solution. Ph.D. thesis, University of Bristol, 1993.
12. Carrington, S. P., Extensional flow of polymer solutions. Ph.D. thesis, University of Bristol, 1995.
13. Treloar, L. K. G., *The Physics of Rubber Elasticity*, 3rd edn. Clarendon Press, Oxford, 1975.
14. Kuhn, W. and Grün, F., *Kolloidzschr.*, 1942, **101**, 248.
15. Peterlin, A., *Pure and Appl. Chem.*, 1966, **12**, 563.
16. Ryskin, G., *J. Fluid Mech.*, 1987, **178**, 423.
17. Rallison, J. M. and Hinch, E. J., *J. Non-Newtonian Fluid Mech.*, 1988, **29**, 37.
18. Wiest, J. M., Wedgewood, L. E. and Bird, R. B., *J. Chem. Phys.*, 1989, **90**, 587.
19. Larson, R. G., *Rheol. Acta*, 1990, **29**, 371.
20. Hinch, E. J., *J. Non-Newtonian Fluid Mech.*, 1994, **54**, 209.
21. *Polymer Handbook*, 3rd edn, ed. J. Brandrup and E. H. Immergut. Wiley Interscience, USA, 1989.
22. De Gennes, P. G., *J. Chem. Phys.*, 1974, **60**, 5030.
23. Tatham, J. P., Carrington, S. P., Odell, J. A., Gamboa, A. C., Müller, A. J. and Sáez, A. E., *J. Rheol.*, 1995, **39**, 961.
24. Hinch, E. J., *Polymères et Lubrification, Colloques Internationaux du CNRS*, 1974, **233**, 241.
25. Harlen, O. G., Hinch, E. J. and Rallison, J. M., *J. Non-Newtonian Fluid Mech.*, 1992, **44**, 229.
26. Bird, R. B., Hassager, O., Armstrong, R. C. and Curtiss, C. F., *Dynamics of Polymeric Liquids*, Vol. 2. Wiley, New York, 1977.